

Ultra-Wideband Analog Optical Signal Processing of Complex Waveforms For Range-Doppler Radar Measurements

Randy R. Reibel and Kristian D. Merkel

Scientific Materials Corporation
2311 S. 7th Ave. Bozeman, MT 59715
reibel@scientificmaterials.com

Zachary Cole, Daryn E. Benson, Tiejun Chang, R. Krishna Mohan and W. Randall Babbitt

Spectrum Lab – Montana State University
2311 S. 7th Ave. Bozeman, MT 59715

Abstract: *Real-time, ultra-wideband (>5 GHz) analog signal processing is experimentally demonstrated utilizing electro-optical devices and spectrally selective optical materials with better than 5 cm range resolution. Doppler resolutions of 125 Hz have been demonstrated. Complex, large time-bandwidth-product analog RF waveforms, including PN codes and band-limited white noise, can be processed from baseband to K-band carriers without down-conversion.*

Keywords: range Doppler correlation; analog optical signal processing; spatial-spectral holography

Introduction

The spectral diversity of radar, communications and electronic warfare continues to expand, as systems employ complex coding and multiplexing schemes. Allocation and use of the available radio frequency spectrum is becoming more dynamic as digital modulation formats aim to employ spread spectrum techniques including the change of carriers, formats and bandwidths depending upon mission needs. As this use of the radio frequency spectrum evolves, there is a need for signal processing systems that can perform matched filtering in real time of complex, dynamic waveforms with large dynamic range and large instantaneous bandwidths, over a broad spectral region.

A traditional antenna receiver chain includes a series of amplification and down-conversion stages acting on the analog signals, each with their own distortions, which can be fed to an analog to digital converter (ADC) with sufficiently high dynamic range. While ADC's are achieving widespread use in receiver chains, they suffer in performance at higher sample rates for signals with ultra-wide instantaneous bandwidths. In a 1999 survey [1], Walden showed that the performance of ADCs falls off with a slope of 1 dB per octave of bandwidth. This trend has not seen significant improvement in recent years, as Walden predicted, despite active research in new materials, such as in SiGe, with a typical specification of 3 or 4 signal-to-noise ratio (SNR) bits at 20 to 40 Gs/s [2,3]. These limitations represent a significant challenge for a receiver chain to processing wide bandwidth complex waveforms with large dynamic range.

Photonic approaches to performing analog signal processing functions offer the potential to alleviate these restrictions. Our approach [4-8] offers a photonic processing device where the RF/microwave signals at the antenna are directly up-converted onto an optical carrier and then processed, rather than being down-converted and digitized. These optical signals then irradiate a spatial spectral (S2) optical memory material, which offers broadband, high dynamic range, real time processing, based upon the ultrawide absorption response of ensembles of narrow linewidth rare earth ions doped into crystalline materials. These S2 materials, in combination with other commercial-off-the-shelf components, can actively perform matched filtering on a variety of complex waveforms in real time to determine delays between waveforms (range processing), as well as coherently integrate multiple results to increase the signal-to-noise ratio and determine frequency shifts between waveforms (Doppler processing).

In this paper, we experimentally demonstrate the flexibility of our optical processor in handling multiple types of complex, high bandwidth waveforms under a variety of conditions. In each demonstration, the 378.13 THz optical transition of a cryogenically cooled Tm:YAG sample ($^3\text{H}_4$ to $^3\text{H}_6$ at 4K) was utilized to process these waveforms without down conversion. New results include processing of: A) pulsed, pseudo-random noise (PN) codes at bit rates between 1-2 GBPS, both at baseband (800 bit codes) and on a 7.8 GHz carrier (1950 bit codes), with single codes repeated for each shot as well as using different codes for each shot at a pulse repetition interval (PRI) of 5 μs , integrated over 10 ms, B) a single, long (~10 ms) 2 GHz band-limited white noise waveform mixed on a 7.8 GHz carrier, C), a single, long (~10 ms) PN code sequence at 2 GBPS, mixed on a 7.8 GHz carrier, and D) pulsed PN codes at 5 GBPS mixed on a 12.5 GHz carrier (4900 bit codes), with codes varied shot to shot at a PRI of 5 μs , and integrated over 10 ms. Physical delays in cases A)-C) at 7.8 GHz were created with a radio frequency (RF) delay line. For case D), the readout bandwidth was >5 GHz, the range accuracy was measured to better than 600 ps, and the root mean square (RMS) of the variance for variable delays was measured to better than 8 ps.

Background on S2 Analog Optical Processing

For analog optical signal processing with S2 materials, coded RF signals are modulated onto a frequency stable optical carrier, through the use of an electro-optic phase modulator (EOPM), which changes the optical carrier phase in proportion to the sign and magnitude of the applied RF voltage. The S2 material processes via absorption in the frequency domain, so that as the light irradiates the material, its absorption creates a frequency dependent two-level atomic population distribution. These spectral features persist as holographic gratings that represent the power spectrum of the combined electric fields over the coherent time-aperture of the material. Consider the interaction of two temporally modulated optical waveforms, $E_1(\tau)$ and $E_2(\tau)e^{i\omega_L\tau_D}$ with a temporal separation τ_D and corresponding phase factor $e^{i\omega_L\tau_D}$ due to the angular frequency of the optical field ω_L , with a S2 material. For radar processing, this represents a transmitted and received radar waveform modulated on an optical carrier. Within the coherence time of the atomic transitions, the combined power spectrum of these pulses over their full bandwidth is recorded as the square of the sum of the electric field amplitudes, which follows as

$$|E_{21}(\omega)|^2 = |E_1(\omega) + E_2(\omega)e^{-i(\omega-\omega_L)\tau_D}|^2 = |E_1(\omega)|^2 + |E_2(\omega)|^2 + E_1^*(\omega)E_2(\omega)e^{-i(\omega-\omega_L)\tau_D} + c.c.,$$

where $E_1(\omega) \leftrightarrow E_1(\tau)$ and $E_2(\omega)e^{-i\omega\tau_D} \leftrightarrow E_2(\tau - \tau_D)$ denote the Fourier transforms. The terms represent the individual power spectra of the first and second waveforms and the interference of both pulses.

Integration of multiple exposures over the persistence time of the atomic transition can strengthen the grating signature and provide enhanced Doppler resolution. A Doppler resolution of 125 Hz has been previously demonstrated [5].

Within the persistence time of the atomic transitions, the S2 grating features can be read out with an appropriate linear frequency modulated (LFM), or chirped, optical waveform [4-8]. This allows a wideband temporal map of the S2 grating to be created in a manner that generates relatively low bandwidth optical intensity modulation, which can be photodetected and digitized with large dynamic range (e.g. a digitizer with 14-16 bits at 100 Ms/s). An apparatus to create a broadband optical frequency chirped pulse can be created by several methods, including using an EOPM driven by a digitally chirped RF source [9], which was utilized here.

The use of a single EOPM for all RF waveforms creates a collinear geometry, resulting in purely spectral gratings, while an angled geometry, which could employ two EOPMs, one for the reference waveform and one for the signal waveform(s) with the light overlapping within the S2 material at a small angle, results in spatial-spectral gratings. The latter approach adds complexity, but introduces

potential benefits [8] that remain to be demonstrated in a future work.

Experimental Demonstrations

Figure 1 (top) shows the experimental setup that was utilized for demonstrations and (middle) a photograph of the actual implementation on the optical table. A frequency stabilized optical carrier at the 378.13 THz Tm:YAG transition is utilized as the source [10]. Laser light was coupled into a single EOPM (a collinear geometry), which was used both to modulate the light with RF waveforms for processing (reference and return signals) and also for creating the readout chirped optical waveform for readout.

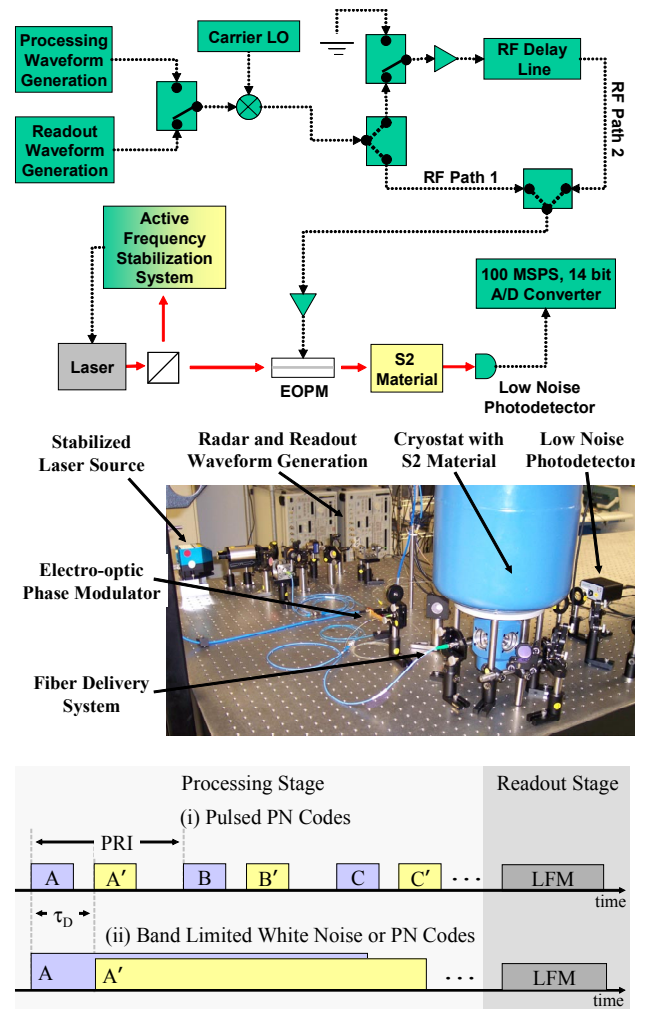


Figure 1. (Top) Experimental schematic showing the RF and optical pathways. (Middle) A photograph of the experimental apparatus used for the demonstrations. (Bottom) A diagram showing the processing and readout stages for two types of experiments, (i) pulsed PN codes and (ii) single long waveforms, which were either band limited white noise or PN codes.

After the EOPM, the light is focused to a $\sim 100\ \mu\text{m}$ spot at the center of the 7 mm long Tm:YAG crystal with a 0.1 atomic percent doping level of Tm, which was cooled to 4K inside an optical cryostat. The transmitted light is subsequently collected with a lens and focused onto a low noise AC coupled photodetector (New Focus 1801), and digitized at 100 MSPS with 14 bits of vertical resolution (National Instruments 5122).

As shown in Figure 1 (bottom and top), proper timing of a fast switch allowed signals to be applied to the single EOPM in two stages, the processing and then the readout stage. For processing, PN codes were created by a pulse pattern generator (PPG; Advantest D3186), and band-limited noise waveforms were created by a noise generator (NoiseCom PNG7112). The RF signal for readout was a LFM tone that was created digitally with a second PPG at a sample rate of 12 GBPS. For RF carrier experiments, a RF mixer was used (MACOM M86C). After mixing, the signals were passed to a RF power divider, where they traveled directly to a recombiner (RF path 1) or to a RF delay line (RF path 2). A switch in this pathway with $>45\ \text{dB}$ of isolation was utilized to prevent signals, such as those for readout, from incurring this time delay. Finally, the signals were combined with a power combiner, amplified (HP83020A) and then fed to the EOPM.

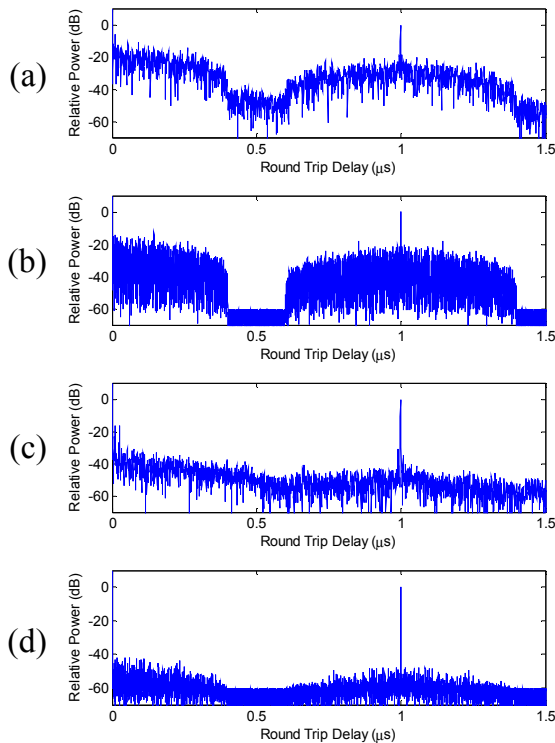


Figure 2. Traces (a) and (c) show experimental results, and (b) and (d) show modeling results for the S2 material response to a baseband 800 bit pulsed PN code sequence at 2 GBPS. For (a)-(b), a single code was used and repeated for every shot, while for (c)-(d) an agile code sequence was used resulting in a suppression of the temporal sidelobe structure.

Baseband Experiments: Figures 2 (a) and (c) show experimental results for the S2 material's response to a sequence of PN coded waveforms at baseband using a PPG operating at 2 GBPS. Here the mock transmit and return pulses were created by electronically repeating the 800 bit PN codes with a delay of $1\ \mu\text{s}$ between them. These mock transmit and return pulses were then repeated at a PRI of $5\ \mu\text{s}$ for 10 ms before being read out as shown in the timing diagram (i) of Figure 1. The readout bandwidth was 1.8 GHz (a LFM waveform from 0.1 to 1.9 GHz at baseband) over $200\ \mu\text{s}$. Two cases are demonstrated. First, the same transmit and return pulses were repeated at the PRI resulting in the delay profile shown in Figure 2 (a). In the second case, shown in Figure 2(c), codes that varied shot to shot (agile codes) were used. For agile codes, the S2 material performs a unique matched filtering operation for each shot. Figures 2 (b) and (d) show simulation results from a computer-based numerical model that takes into account the S2 material's physical response to the coded sequences of (a) and (c). For (a)-(d), a correlation peak is observed at the delay time and an autocorrelation peak at zero delay. Code dependent temporal sidelobes are apparent in (a) and (b) due to the use of the single code repeated in the sequence, while in (c) and (d) this structure is suppressed through the integration of different sidelobe structure for each shot. For this agile coding, the actual sidelobe structure is expected at a RMS relative power level of $-61\ \text{dB}$, which falls below the experimental and simulated noise floor, however some sidelobe structure is still visible in both the experiment and the modeling.

7.8 GHz Delay Line Experiments: A set of experiments was conducted to demonstrate radar range processing for a variety of waveforms, including band limited white noise and PN codes, utilizing a bulk acoustic wave RF delay line

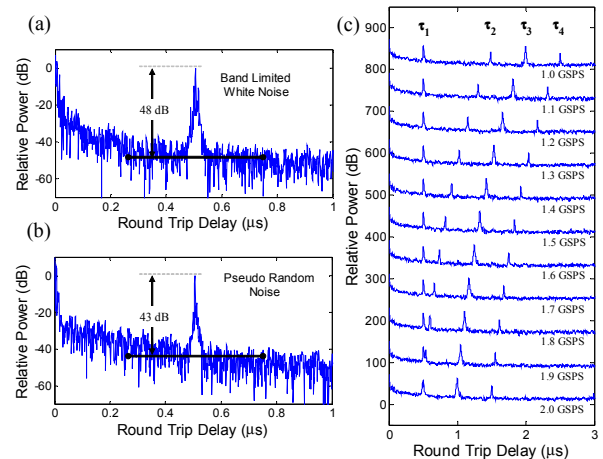


Figure 3. Range processing results using a RF physical delay line of $\tau_1 \sim 0.5\ \mu\text{s}$, for (a) a 2 GHz, 10 ms band limited white noise waveform, (b) a 2 GBPS, 10 ms PN coded waveform, and (c) a pair of two PN coded waveforms of 1950 bits, resulting in a set of four delays, where τ_1 was fixed and τ_2 , τ_3 and τ_4 varied depending upon the bit rate of the waveform generator between 1.0 and 2.0 GBPS.



Figure 4. (Left) Range processing results for a set of dynamic 4900 bit PN codes modulated at 5 GBPS and readout over 5 GHz. The peak value had a measurement error of ~ 600 ps and a 3 dB full width of 303 ps, giving range resolution of < 5 cm. (Right) A plot of measured delays versus programmed relative delays, showing a RMS of the variance that is better than 8 ps over the 2.6 ns delay variation.

(Teledyne Wireless MBH-1015) to mimic a target delay of ~ 0.5 μ s. This device had a specified 1 GHz of bandwidth at a 7.8 GHz (C-band) carrier frequency. The readout bandwidth was 2 GHz (a LFM waveform from 0.05 to 2.05 GHz mixed on the 7.8 GHz carrier) over 200 μ s. Figure 3(a) shows the range processing results for a 2 GHz band limited white noise waveform, time-gated for ~ 10 ms and mixed on a 7.8 GHz carrier, which propagated through both RF path 1 (transmit waveform) and RF path 2 (delayed replica waveform). The main delay peak is found at a measured delay of 0.507 μ s with 48 dB of SNR measured from the peak to the RMS noise floor for the region shown. The broad peak structure is likely due to dispersive effects in the RF path. Figure 3(b) shows similar results for a long, single PN code at 2 GBPS, created over ~ 10 ms by the PPG under the same conditions. The peak is found at 0.507 μ s with 43 dB of SNR measured as in (a).

A third delay line demonstration was performed with pulsed PN codes, using both the fixed delay from the RF delay line and a controllable electronic delay imposed by the PPG. For this case, a code and its replica, each 1950 bits long with 2000 bits of delay between them, were created by the PPG and mixed on a 7.8 GHz carrier. Agile codes were used shot to shot at a PRI of 5 μ s and integrated for ~ 10 ms, before readout (as shown in the timing diagram of Figure 1). This bit sequence created a delay of $\tau_3 = 2000/\Gamma_{PPG}$, where Γ_{PPG} is the bit rate of the PPG. These codes also were propagated through the delay line path, giving a total of four apparent delays where τ_1 is the delay of the delay line, and τ_2 and τ_4 are the programmed delay, τ_3 , minus or plus τ_1 respectively. Figure 3 (c) shows the correlation peaks for each of these four delays with values for Γ_{PPG} ranging from 1.0 GBPS to 2.0 GBPS in steps of 0.1 GBPS.

12.5 GHz Range Accuracy and Resolution Experiments:

Another experiment was performed using a 12.5 GHz (Ku band) carrier to illustrate high range resolution and

accuracy. A 4900 bit long PN code and its replica were modulated at 5 GBPS with an electronic coded time delay of 0.9998 μ s between them (4999 bits), with codes changing shot to shot (agile sequence) at a PRI of 5 μ s over ~ 10 ms. The readout bandwidth was 5 GHz (a LFM waveform from 0.05 to 5.05 GHz mixed on the 12.5 GHz carrier) over 500 μ s. Figure 4 (left) shows the range processing result, where the main delay peak was observed at 0.9992 ms, a measurement error of ~ 600 ps, or 0.06%. The main peak had a 3 dB full width (3dB FW) of 303 ps, providing range resolution of ~ 4.5 cm. Finally, the bit rate of the PPG was stepped by 1 MHz and 100 kHz increments, providing temporal steps of ~ 200 ps and ~ 20 ps, respectively. Under these conditions, the relative delay change with respect to the initial peak at 5 GBPS was observed and plotted in Figure 4 (right) as measured delay versus programmed relative delay. A linear trend is observed, as expected, and a best fit line provides a unity slope with a RMS of the variance that is better than 8 ps over the 2.6 ns delay variation.

Acknowledgements

The authors would like to thank A. Olson and B. Litersky of Montana State University for discussions and their help with RF components used in the experiments.

References

1. R.H. Walden, IEEE Journal on Selected Areas in Communications, vol. 17 pp. 539-550, April 1999.
2. F. Stroili, J. Huggett, D. Jansen, R. Elder, D. Rowe, M. Vadipour, R. Chan, M. Feng, Proc. of GomaticTech, Monterey, CA (2004).
3. W. Cheng, R. Stevens, F. Rupp, C. Engels, W. Ali, M. Choi, D. Devendorf, S. Ding, L. Linder, K. Liu, T. Tat, Proc. of GomaticTech, Monterey, CA (2004).
4. Z. Cole, T. Böttger, R. Krishna Mohan, R. Reibel, W. R. Babbitt, R. L. Cone and K. D. Merkel, Appl. Phys. Lett. 81, 3525 (2002).
5. W. R. Babbitt, T. Harris, K. D. Merkel, R. K. Mohan, Proceedings of CLEO, San Francisco, CA (2004).
6. K. D. Merkel, R. Krishna Mohan, Z. Cole, T. Chang, A. Olsen and W. R. Babbitt, J. Lum. 107 62-74 (2004).
7. K. D. Merkel, Z. Cole, R. K. Mohan, and W. R. Babbitt, Proc. of GomaticTech, Tampa, FL (2003)
8. T. Chang, R. K. Mohan, M. Tian, T. L. Harris, W. R. Babbitt, and K. D. Merkel, Phys. Rev. A. 063803 (2004)
9. R. Reibel, Z. Barber, J. Fischer, M. Tian, W. R. Babbitt, J. Lum. 107, 103-13 (2004).
10. N. M. Strickland, P. B. Sellin, Y. Sun, J. L. Carlsten, and R. L. Cone, Phys. Rev. B 62, 1473 (2000)